Surface & Coatings Technology 402 (2020) 126326

Contents lists available at ScienceDirect

Surface & Coatings Technology

journal homepage: www.elsevier.com/locate/surfcoat

Performance and local structure evolution of NbMoTaWV entropy-stabilized oxide thin films with variable oxygen content

Linxia Bi[a], Xiaona Li[a,*], Zhumin Li[a], Yinglin Hu[a], Junyi Zhang[a], Qing Wang[a], Chuang Dong[a], Yuehong Zheng[b], Peter K. Liaw[c]

[a] Key Laboratory of Materials Modification by Laser, Ion and Electron Beams (Ministry of Education), School of Materials Science and Engineering, Dalian University of Technology, Dalian 116024, China
[b] State Key Laboratory of Advanced Processing and Recycling of Nonferrous Metals, Lanzhou University of Technology, Lanzhou 730050, China
[c] Department of Materials Science and Engineering, The University of Tennessee, Knoxville, TN 37996, USA

ARTICLE INFO

Keywords:
Entropy-stabilized oxide
Refractory high-entropy film
Cluster-plus-glue-atom
Hardness
Resistivity

ABSTRACT

Entropy-stabilized refractory metal oxide thin films have great application prospects in many fields due to their good preparation performance, excellent thermal stability, high hardness and abrasion resistance, and adjustable conductivity. In present paper, a series of $(NbMoTaWV)_{100-x}O_x$ (x = 0–53.63) five-component entropy-stabilized oxide thin films were deposited on the single-crystal Si (100) substrates by radio frequency magnetron sputtering to study the effect of oxygen content on their performance and local structure. With increasing the oxygen content, the films gradually transform from body-centered-cubic solid solutions to the amorphous oxides. The hardness and modulus of the films obtain a maximum of 15.5 GPa and 215.6 GPa, respectively. The room temperature resistivity can be tuned in the range of 55–1.26×10^6 μΩ·cm, and the trends of the resistivity-temperature behavior of the films have significant differences. Films with low oxygen contents show good resistivity stability in a wide temperature range. Simultaneously, the conductive mechanism gradually changes from the metallic type to amorphous oxide semiconductor type (a near TiO_2 type ionic crystal type) as the oxygen content increases. The cluster-plus-glue-atom model has been introduced to interpret the composition of films, and the relationship between the variations of the local structure and strengthening (or conduction) mechanism is discussed in detail. Here, the performance of $(NbMoTaWV)_{100-x}O_x$ films can be modulated in a large range (covering conductors to semiconductors), which provides a broad prospect for the application of refractory high-entropy oxide films.

1. Introduction

Entropy could drive a reversible solid-state transition between multiphase and single-phase state which has been proved by Rost et al. [1,2]. That is, the five equimolar metal oxides (MgO, CoO, NiO, CuO, and ZnO) could be transformed into a single phase five-component oxide, and the cation distributions are random and uniform. The new five-component oxides not only contain the high configurational entropy but also is indeed truly entropy stabilized, which belongs to the ions compound category.

Compared with the single cationic-metal oxide, the entropy-stabilized poly-cationic metal oxide with five or more cations has more excellent performance. For instance, the hardness of $(AlCrNbTaTi)O_2$ film can reach 22–24 GPa while those of the TiO_2 and Al_2O_3 films are only up to 13 GPa and 9 GPa, respectively [3–5]. Furthermore, entropy-stabilized oxides have several special properties due to multi-component mixing, e.g., (MgCoNiCuZnO) thin films exhibit the high reversible capacity, long-term cycle stability and excellent rate performance as negative electrode materials of lithium-ion batteries [6], and also have the unique near-minimum thermal conductivity, high elastic modulus, superior mobility and large dielectric constants [2,7,8]. $(FeMgCoNi)O_x$ oxides have the ability of thermochemical water splitting [9].

In recent years, many investigators are concerned on entropy-stabilized oxides due to their advantages given by multi-component mixing. However, there are more issues worth addressing, e.g., the entropy-stabilized oxide with a stoichiometric ratio of 1:1 between the metal and oxygen is an ionic-crystal compound [1], but as the oxygen content changes, whether the high-entropy oxide is still an ionic crystal,

* Corresponding authors at: Key Laboratory of Materials Modification by Laser, Ion and Electron Beams, The Ministry of Education, Dalian University of Technology, No. 2 Linggong Road, Dalian 116024, China.
E-mail address: lixiaona@dlut.edu.cn (X. Li).

https://doi.org/10.1016/j.surfcoat.2020.126326
Received 8 April 2020; Received in revised form 22 June 2020; Accepted 19 August 2020
Available online 21 August 2020

and what is the evolution trend of its performance and structure.

As one of the typical entropy-stabilized oxides, the refractory high-entropy oxide exhibits excellent thermal stability [10,11]. However, it is prepared difficultly by the conventional method due to the high melting point of elements. Fortunately, this difficulty can be overcome by the preparation of thin films. In many thin film deposition techniques, magnetron sputtering, which is a suitable thin film deposition technology for the large-scale production due to its uniform and dense film formation, provides greater possibilities for the application of refractory high-entropy oxides [12,13]. Particularly, the composition of films can be controlled by adjusting the oxygen partial pressure.

Furthermore, previous studies [3,14] have indicated that refractory high-entropy oxide films can be used as protective layers for processing tools and components since they withstand high temperatures and mechanical loads. For instance, $(AlCrNbTaTi)O_2$ film can maintain the mono-phase crystallization of a rutile structure after annealing at 1200 °C and exhibit high hardness and modulus values of 22–24 GPa and 380–410 GPa, respectively [3]. The $(AlCrTaTiZr)O_x$ film remains amorphous after annealing at 800 °C for 1 h, and its hardness and modulus can reach 20 GPa and 260 GPa, respectively [14]. However, the stoichiometry of metal and oxygen elements in these films with excellent properties is different.

Therefore, it is necessary to further explore the influence of oxygen content on the properties and structures of refractory high-entropy oxide films, and to select appropriate metal components for the preparation of samples with different oxygen contents. It is well known that the high-entropy alloy usually has a relatively-simple single-phase structure, such as face-centered cubic (FCC), body-centered cubic (BCC), and hexagonal close-packed (HCP) [15,16]. Typically, the high-entropy alloy consisting of five refractory metal elements, Nb, Mo, Ta, W, and V, has a single BCC structure [17], which has a relatively-large octahedral gap and can solute small atoms easily. Thus, utilizing the three characteristics of the good stability introduced by refractory elements, single BCC structure, and large lattice gap, it can be determined that the NbMoTaWV high-entropy alloy is suitable to the preparation and research of entropy-stabilized oxides with varying oxygen contents. Besides, studies about NbMoTaWV thin films are focused on their oxidation resistance [18,19]. The properties of NbMoTaWV oxides and the effect of oxygen content on the film have not been systematically investigated.

In the present paper, $(NbMoTaWV)_{100-x}O_x$ films with varying oxygen contents were prepared by magnetron sputtering, and their microstructures, compositions, microhardness, room-temperature (RT) resistivity, and variable temperature resistance were characterized. Furthermore, the cluster-plus-glue-atom model [20] was introduced to interpret the composition, and the effects of variable oxygen contents on local structures, properties, strengthening mechanisms and conductivity mechanisms were systematically discussed, which lays a good foundation for the application of refractory high-entropy oxides in high-temperature, wear-resistance, and microelectronics fields.

2. Material and methods

A series of refractory high-entropy $(NbMoTaWV)_{100-x}O_x$ films were deposited on single-crystal Si (100) substrates with a JGP450 magnetron sputtering system. The sputtering target was a Nb-Mo-Ta-W-V five-element alloy combination target, which was composed of a hot-pressing target (Φ75 mm × 3 mm) of Nb-Mo-Ta-W quaternary powders with equal atomic ratio and six pure vanadium pieces (Φ8 mm × 1 mm) pasted in the main sputtering area of a quaternary target. Purity of each component was not less than 99.9 wt%. Thin films were prepared by the radio frequency (RF) power supply operated at 100 W. The background vacuum was $< 3.0 \times 10^{-4}$ Pa. There was 40 min pre-sputtering, followed by 90 min formal sputtering, and the substrate temperature was not higher than 323 K. Different composition oxide films were prepared by controlling the ratio of oxygen and argon with a total gas flow of 30 sccm (standard cubic centimeter per minute).

The chemical composition analysis was analyzed with the Electron Probe Micro-analyzer (EPMA, EPMA-1600, Shimadzu, Japan), in which wavelength dispersive spectrometer (WDS) with a resolution of 5eV, low detection limit (0.01–0.05%) and wider detectable element range (4Be-92U) is suitable for quantitative analysis of the element. In this study, considering that oxygen is a light element, the detection precision may not reach 0.01–0.05% due to low count rate [21]. The expression relating to oxygen content in the paper is to keep a unified form with other metal elements, but its true precision may be less by an order of magnitude compared with other elements. The energy-dispersive x-ray spectroscopy (EDS) of the scanning transmission electron microscopy (STEM, FEI Tecnai G^2, the United States) and Auger electron spectroscopy (AES, PHI-700, ULVAC-PHI, Japan) were used to analyze the compositional distributions of the thin films. The microstructures of thin films were analyzed, using a Grazing-angle incidence X-ray diffraction (GIXRD, Bruker D8 Discover, Karlsruhe, Germany; grazing angle: 1°), and a transmission electron microscope (TEM, Philips Tecnai G^2, Amsterdam, the Netherlands). The high-resolution mode of TEM (HRTEM) was conducted to investigate the nanocrystals of the films. TEM samples were prepared by Ar-ion milling using a Gatan precision ion polishing system (PIPS-691, Pleasanton, the United States). The thicknesses were measured by a scanning electron microscope (SEM, Zeiss Supra55, Baden-Wurttemberg, Germany).

The hardness and elastic modulus of thin films were measured by a nano-indenter (XP, MTS, the United States). The RT resistivity of the thin films were measured again by a four-point probe tester (RTS-9, 4 Probes Tech, Guangzhou, China). The resistivity-temperature measurements were carried out with a variable temperature resistivity meter (TRT-1000, Wuhan, China), the testing temperature increased from RT to 1078 K, with a constant heating rate of 10 K/min.

Table 1
Chemical compositions and thicknesses of $M_{100-x}O_x$ films.

Samples	Chemical composition (at. %)						Nb:Mo:Ta:W:V (atomic ratio)	Film thickness (nm)
	Nb	Mo	Ta	W	V	O		
M	18.37	17.87	18.67	20.61	24.74	0	1:1:1:1.1:1.4	478
$M_{91.84}O_{8.16}$	16.67	16.42	16.96	18.36	23.42	8.16	1:1:1:1.1:1.4	465
$M_{83.63}O_{16.37}$	14.97	15.25	15.19	16.57	21.61	16.37	1:1:1:1.1:1.4	503
$M_{78.46}O_{21.54}$	14.33	14.69	14.44	16.58	18.41	21.54	1:1:1:1.1:1.4	603
$M_{64.08}O_{35.92}$	11.75	11.59	11.86	13.24	15.65	35.92	1:1:1:1.1:1.3	638
$M_{56.80}O_{43.20}$	10.49	10.59	10.55	11.70	13.47	43.20	1:1:1:1.1:1.3	650
$M_{49.07}O_{50.93}$	9.01	9.03	9.27	10.22	11.54	50.93	1:1:1:1.1:1.3	730
$M_{46.37}O_{53.63}$	8.62	8.73	8.72	10.16	10.14	53.63	1:1:1.1:1.2:1.2	796

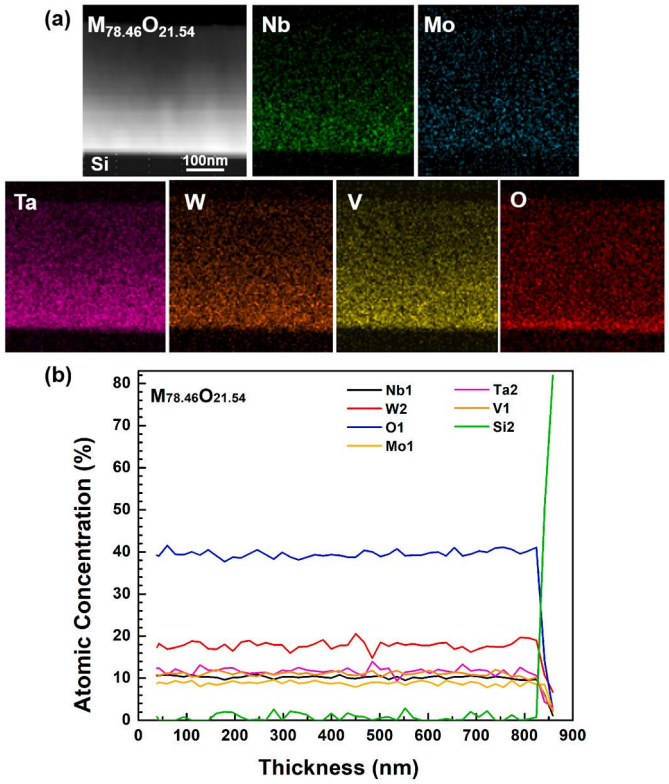

Fig. 1. Cross-sectional STEM-HADDF image, EDS elemental mappings (a), and AES depth profile (b) for the as-deposited $M_{78.46}O_{21.54}$ thin film.

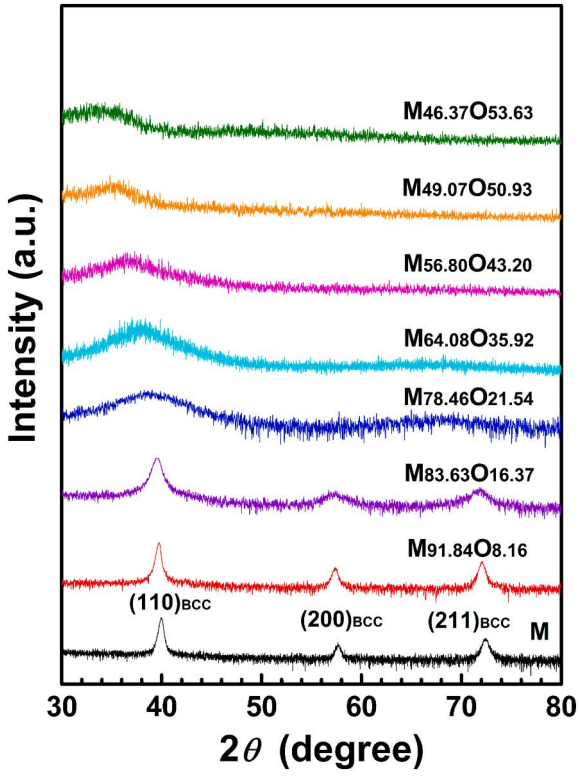

Fig. 2. GIXRD patterns of the as-deposited $M_{100-x}O_x$ (x = 0–53.63) thin films.

3. Results

3.1. Compositions and microstructures of thin films

Table 1 shows the compositions (measured by EPMA) and thicknesses (determined with the cross-sectional SEM image) of the as-deposited thin films. The oxygen content ranges from 0 to 53.63 atomic percent (at.%). The atomic ratio of the metal components can be calculated according to their content. Only the proportion of vanadium is slightly higher, and the other elements are approximate equimolar ratios. Furthermore, there is a slight change in the composition ratio under different oxygen partial pressures. The proportion of vanadium gradually decreases but that of tungsten slightly increases with increasing the oxygen partial pressure due to the different sputtering thresholds and rates of the elements. The thickness increases with the increase of the oxygen partial pressure, which is 478 nm in the oxygen-free state, and can reach up to 796 nm when the oxygen content increases to 53.63 at.%. For convenience, the part of the metal component (NbMoTaWV) is marked as "M", and the films are collectively labeled as $M_{100-x}O_x$ (x = 0–53.63).

The cross-sectional high-angle annular dark field (HAADF) image of the as-deposited $M_{78.46}O_{21.54}$ film was obtained through STEM [Fig. 1(a)], the film shows a uniform thickness and a smooth film-substrate interface. The distribution of elements is random and uniform in the film according to the EDS elemental mappings [Fig. 1(a)] and the AES depth profile [Fig. 1(b)], which meets the chemical disorder characteristics of high-entropy alloys. In addition, the AES test is based on the change of the intensity of a characteristic peak of the element with the profiling depth to determine whether the distribution of the element in the vertical direction of the film is uniform, so the percentage content does not represent the actual element content.

Fig. 2 shows the GIXRD patterns of the as-deposited $M_{100-x}O_x$ (x = 0–53.63) thin films. It can be seen that the oxygen-free thin film has a single-phase BCC structure, and the diffraction peaks at 39.5°, 57.0° and 72.0° correspond to the (110), (200), and (211) crystal planes, respectively. Moreover, the broad diffraction peaks indicate that the grains are relatively small. From oxygen-free state to the oxygen content of 16.37 at.%, the films maintain the BCC structure, but the width of the diffraction peaks increases gradually. When the oxygen content reaches 21.54 at.%, only two broad diffraction peaks remain in the range of 30–80°, which is a manifestation of the continuous reduction in grain size. Further increasing the oxygen content, the films have only a single broad diffraction peak. However, whether the films are amorphous or of fine nanocrystalline structures requires the determination by TEM. The diffraction peaks significantly shift to the left with the increase of the oxygen content, which is an intuitive manifestation of the lattice expansion caused by the oxygen as interstitial atoms dissolved into the BCC lattice. Moreover, the film stress increases with the increase of the oxygen solid solution.

Fig. 3 shows TEM analysis results of the as-deposited M, $M_{91.84}O_{8.16}$, and $M_{83.63}O_{16.37}$ thin films. The cross-sectional morphologies of the three films are basically the same, all of which show columnar crystal, and have a smooth film-substrate interface with uniform thickness. As an example, Fig. 3(a_0) displays the cross-sectional morphology of the as-deposited M film. Fig. 3(a_1–c_1) and (a_2–c_2) exhibit the planar bright-field and dark-field images of the three films. The average grain size decreases slightly with increasing oxygen content. For the M film, it is about 42 nm measured by Nano Measurer 1.2 software [22]. The three films are identified as single-phase BCC structures by selected area electron diffraction (SAED) patterns [Fig. 3(a_3–c_3)], which are consistent with XRD results. However, the diffraction rings become continuous with increasing oxygen content, and they are blurred and broadened when the oxygen content reaches 16.37 at.%, further indicating that the grain size gradually becomes smaller.

The cross-sectional TEM analysis results of the as-deposited $M_{78.46}O_{21.54}$, $M_{64.08}O_{35.92}$ and $M_{46.37}O_{53.63}$ thin films are shown in Fig. 4. The film-substrate interfaces are smooth and the films are free of columnar crystals [Fig. 4(a_1–c_1)]. The HRTEM image shows that the $M_{78.46}O_{21.54}$ film is composed of fine crystallites (about 4 nm), which is

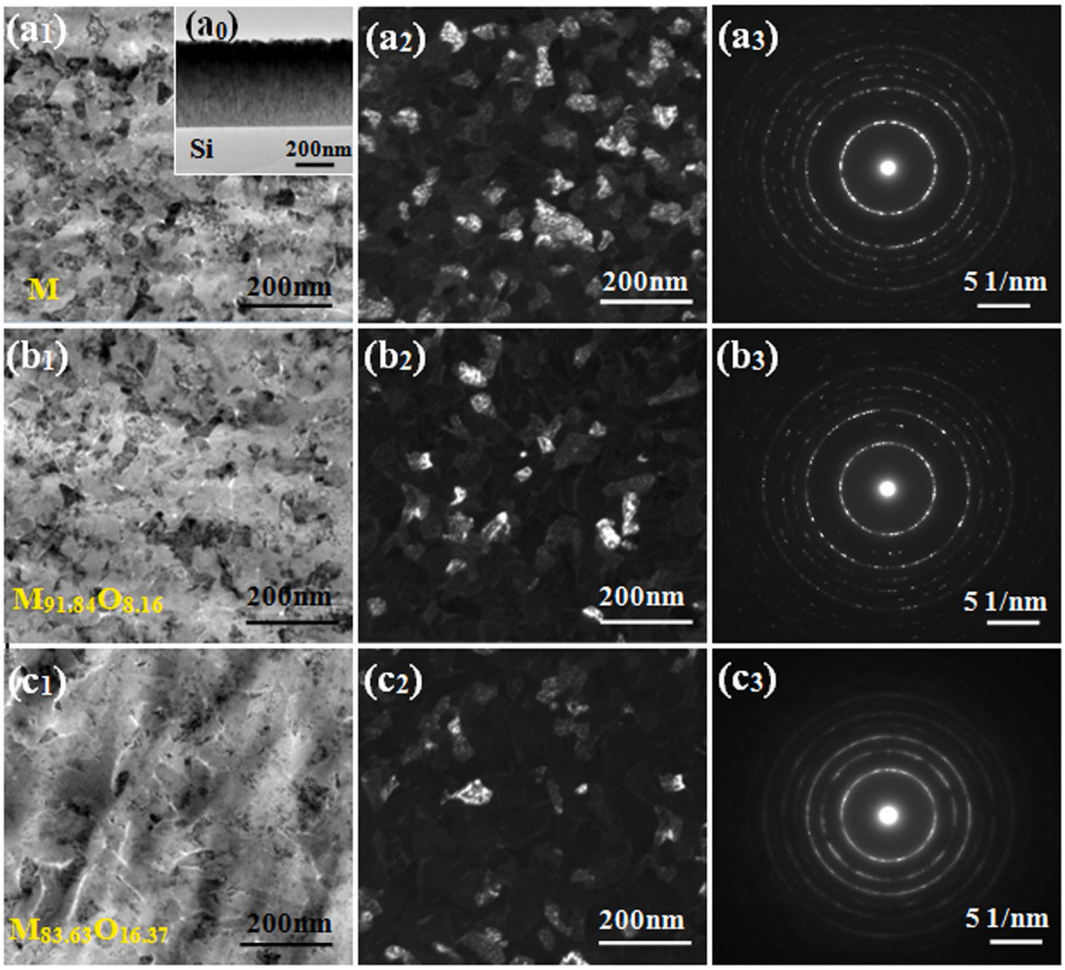

Fig. 3. Cross-sectional TEM bright-field image of the as-deposited M (a_0). Planar bright-field images (a_1–c_1), dark-field images (a_2–c_2), and SAED patterns (a_3–c_3) of the as-deposited M, $M_{91.84}O_{8.16}$, $M_{83.63}O_{16.37}$ thin films.

a BCC structure according to the fast Fourier-transform (FFT) analysis [the insert on the bottom right corner of Fig. 4(a_2)]. For the $M_{64.08}O_{35.92}$ film, some amorphous regions appear in the nanocrystalline gaps [Fig. 4(b_2)]. The $M_{46.37}O_{53.63}$ thin film is a completely-amorphous structure [Fig. 4(c_2)]. Furthermore, the SAED patterns shows that the $M_{78.46}O_{21.54}$ and $M_{64.08}O_{35.92}$ thin films have a wide diffraction ring and several weak ones [Fig. 4(a_3–b_3)], which are consistent with diffraction characteristics of nanocrystallites. The $M_{46.37}O_{53.63}$ thin film shows a typical amorphous electron diffraction pattern. Obviously, films gradually change from a single-phase BCC structure to an amorphous oxide with increasing the oxygen content. It is worth mentioning that the average radius of the first diffuse wide ring of the $M_{46.37}O_{53.63}$ thin film is significantly smaller than those of the other two films, which indicates that the local structure has changed.

3.2. Compositional interpretation of thin films

Whether in crystal or amorphous, there is a strong interaction between neighboring atoms, leading to the generation of the short-range-order, which can be described through an intuitive way of the first nearest-neighbor coordination polyhedral (cluster) [23,24]. Dong et al. [20] proposed a cluster-plus-glue-atom model based of the nearest-neighbor coordination polyhedra. According to this model, any phase structure can be described by a universal cluster formula, [cluster](glue atoms)$_x$, where x is the number of glue atoms.

Here the cluster should be the one that best represents the local short-range-order feature of the structure, termed “principal cluster” to distinguish it from multiple clusters present in a given structure, which should be the most strongly bounded part in the structure [25]. Meanwhile it can be inherited after the phase transition because of its strong stability. The glue atom position is located on the second nearest-neighbor shell [26]. Therefore, the model actually describes the main chemical local structure and topological structure, this kind of molecular formula shows the local short-range-order characteristics of the phase structure [27].

The oxygen-free NbMoTaWV thin film has a single-phase BCC structure. According to the cluster selection principle, the cluster model of the BCC structure is: [(center atom)-(shell atom)$_{14}$]-(glue atom)$_x$, x being the integer number of glue atoms matching one cluster [28]. The BCC cluster model has been presented in detail in the reference [29]. Here the number of glue atoms chose to be 3, and the first 8 and the last 6 atoms closest to the central atom form a diamond decahedron as the principal cluster [m-m_{14}], where the m represents the random positions of five metal atoms (Nb, Mo, Ta, W, and V), the schematic diagram is shown in Fig. 5(a). For the NbMoTaWV alloy system, the five elements are randomly occupied in the cluster, which can be regarded as a mixture of five atoms.

Ideally, oxygen can be dissolved in the interstitial space of the crystal lattice, forming an octahedral interstitial solid solution, which derives from the difference in the atomic radius (the atomic radius of oxygen is 0.66 Å, while those of Nb, Mo, Ta, W and V are all between 1.35 Å and 1.47 Å). This form of atomic occupancy is the most stable, which is attributed to the strong interactions between the oxygen and the other five elements caused by a large negative mixing enthalpy

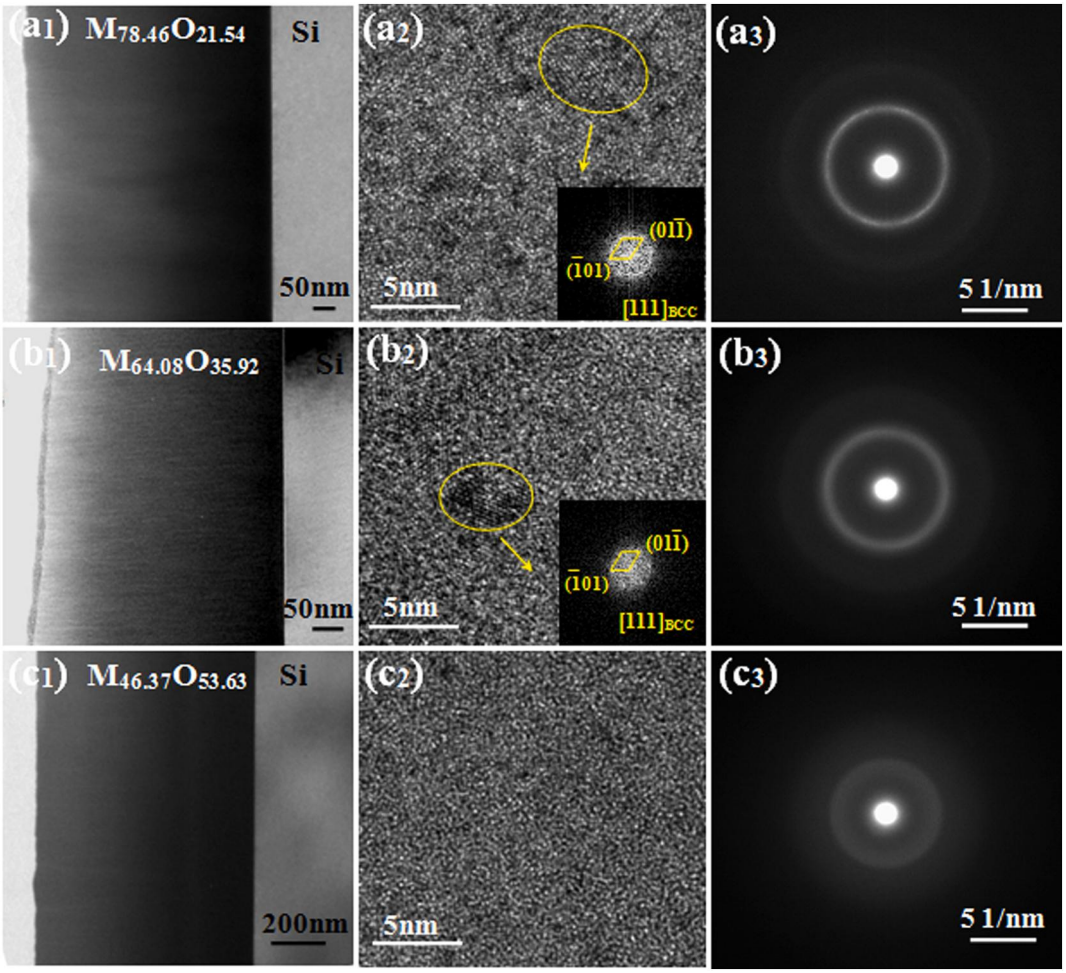

Fig. 4. Cross-sectional bright-field TEM images (a_1–c_1), HRTEM images and corresponding FFT patterns (a_2–c_2), SAED patterns (a_3–c_3) of the as-deposited $M_{78.46}O_{21.54}$, $M_{64.08}O_{35.92}$, $M_{46.37}O_{53.63}$ films.

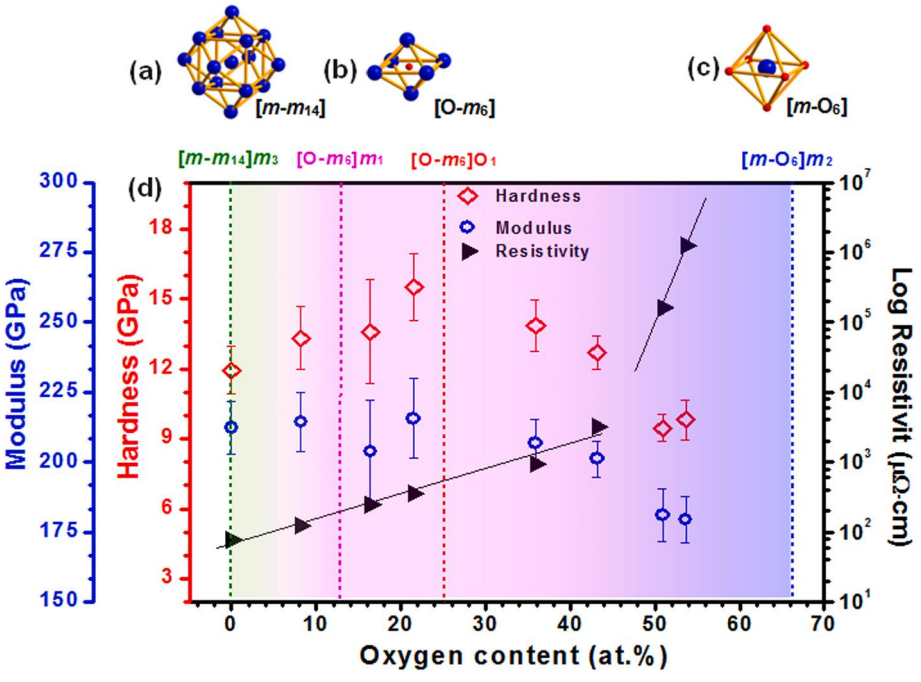

Fig. 5. Schematic diagrams of clusters: [m-m_{14}] (a), [O-m_6] (b) and [m-O_6] (c). (The big blue solid circles represent the random positions of five metal atoms (Nb, Mo, Ta, W and V), the small red solid circles represent the positions of oxygen atoms). Hardness, modulus, and resistivity of $M_{100-x}O_x$ (x = 0–53.63) thin films change with the oxygen content and local structure (d). (For interpretation of the references to colour in this figure legend, the reader is referred to the web version of this article.)

between them. Then a cluster model [O-m_6]m_1 with [O-m_6] as the principal cluster [Fig. 5(b)] can be constructed. Obviously, the [m-m_{14}] and [O-m_6] clusters coexist in films with low oxygen contents (< 12.5 at.%). The oxygen-containing clusters will increase with increasing the oxygen content. Once the oxygen content reach up to 12.5 at.%, the film contains only [O-m_6]m_1. Further increasing the oxygen content, the principal clusters do not change but the cluster model translates to [O-m_6]O_1 because oxygen starts to occupy the position of the glue atom.

When the oxygen content is 25 at.%, the solid-solution oxygen content of the BCC structure reaches the maximum. If the oxygen content continues to increase, the local structure of oxygen elements adjacent to each other will inevitable. The local structure will have to be adjusted to the [m-O_6]m_2 cluster formula with m as the center atom [Fig. 5(c)] owing to the constraints of the mixing enthalpy, which is a typical TiO_2-type metal oxide-cluster model rather than other structure types [26]. The reason will be discussed in the discussion section. When the oxygen content is between 25 at.% and 66.7 at.%, the [O-m_6] and [m-O_6] clusters coexist in the thin films. Increasing the oxygen content to 66.7 at.%, the thin film is only consisted of [m-O_6]m_2. All single cluster formulas (local structure) and corresponding component points are marked in Fig. 5(d).

3.3. Performance analysis of thin films

3.3.1. Room-temperature performance

The RT properties (hardness, modulus, and resistivity) of the as-deposited $M_{100-x}O_x$ (x = 0–53.63) films as functions of the oxygen content and local structure are plotted in Fig. 5. Here, in order to exclude the influence of the surface or matrix effect, the value of 1/7 of the film thickness is taken as the measured values in the hardness and modulus curves with the indentation depth, as presented in Fig. 6. The hardness and modulus increase first and then decrease with increasing oxygen content (Fig. 5). For the oxygen-free M film, the values are 11.93 ± 1.02 GPa and 212.12 ± 9.32 GPa, respectively. But those of the film with the maximum oxygen content are 9.82 ± 0.85 GPa, 179.41 ± 8.32 GPa. The hardness of the $M_{78.46}O_{21.54}$ film can reach the maximum of 15.5 ± 1.44 GPa.

In order to visualize the RT-resistivity trend of the $M_{100-x}O_x$ (x = 0–53.63) films, the logarithm values of resistivity as a function of oxygen content are plotted in Fig. 5(d). The resistivity increases with increasing the oxygen content. Those of the oxygen-free and $M_{56.8}O_{43.2}$ films are 77.58 μΩ·cm and 3161.79 μΩ·cm, respectively. However, once the oxygen content is > 43.2 at.%, the resistivity increases sharply, and the maximum value reaches 1.26 × 10^6 μΩ·cm, which belongs to the category of amorphous semiconductors. In the two stages of O at. % ≤ 43.2 at.% and O at.% > 43.2 at.%, different resistivity change

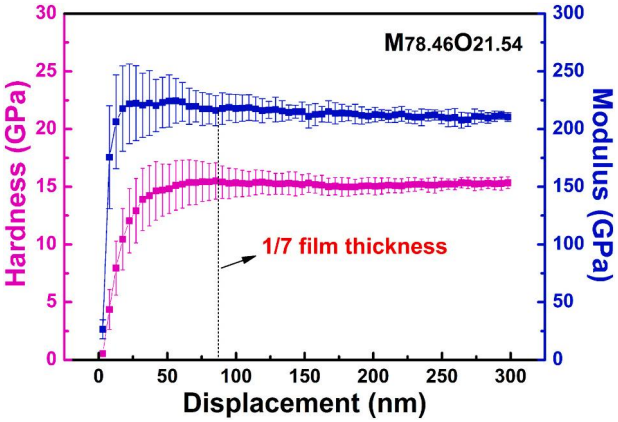

Fig. 6. Hardness and modulus of the $M_{78.46}O_{21.54}$ thin film as a function of the depth of indentation, as well as positions of hardness and modulus values.

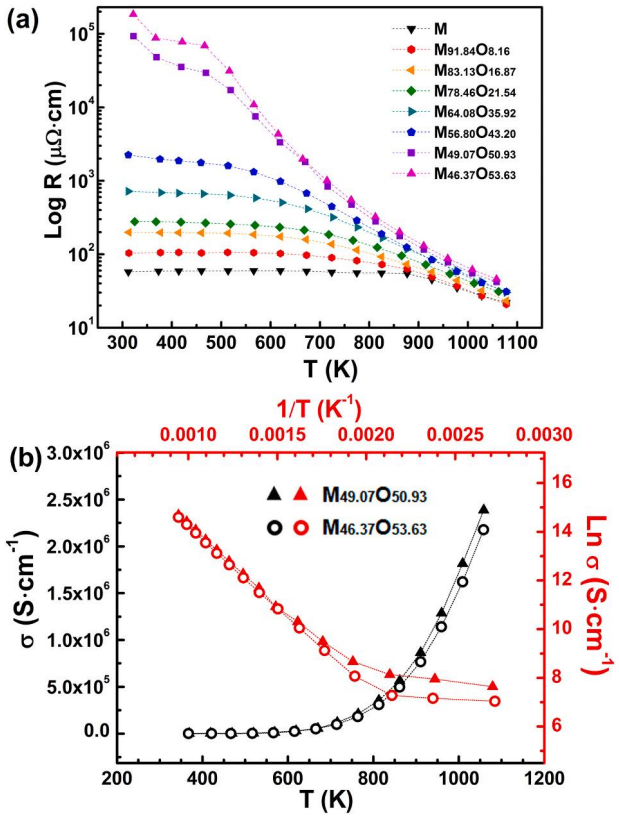

Fig. 7. Resistivity-temperature curves of the as-deposited $M_{100-x}O_x$ (x = 0–53.63) thin films (a). Conductivity-temperature (σ - T) and Lnσ - 1/T curves for the $M_{49.07}O_{50.93}$ and $M_{46.37}O_{53.63}$ thin films (b).

slopes are shown, which are 0.037 and 0.332 (logμΩ·cm/%), respectively. The latter is an order of magnitude larger than the former.

3.3.2. Variable temperature resistivity

The resistivity of the $M_{100-x}O_x$ (x = 0–53.63) thin films during the temperature increase from 373 to 1073 K was measured with a variable temperature resistivity tester. As shown in Fig. 7 (a), the logarithm of the resistivity value was taken as the ordinate due to the large span of resistivity value for the films with different compositions. When the oxygen content is lower than 43.2 at.%, resistivity-temperature curves are divided into two stages. In the first stage, the curves exhibit “plateaux” starting from RT, that is, the resistivity shows little variation with increasing temperature. Especially, the resistivity of the oxygen-free film can stay stable from RT to nearly 873 K, indicating an excellent resistivity stability. In the second stage, the resistivity decreases with increasing temperature, which can drop below 50 μΩ·cm at 1073 K.

However, the “plateaux” disappear in the first stage when the oxygen content reaches 50.93 at.% and 53.63 at.%. The resistivity values of $M_{49.07}O_{50.93}$ and $M_{46.37}O_{53.63}$ films are much higher than those of the low-oxygen films, the former belongs to the category of amorphous semiconductors. In order to further study the conductive behavior at this stage, the conductivity-temperature (σ - T) curves of the two films are plotted in Fig. 7(b), as presented by the black lines, the conductivity increases exponentially with increasing temperature. Taking the logarithm of the conductivity value as the ordinate, the Lnσ - 1/T curves show two different slopes in the range of 373–525 K and 525–1073 K, as exhibited by the red line in Fig. 7(b). According to the literatures [30,31], the amorphous $M_{49.07}O_{50.93}$ and $M_{46.37}O_{53.63}$ thin films have a resistivity-temperature behavior similar to the conductivity of ionic crystals as function of the temperature. These two slopes correspond to the impurity conductivity in the low-temperature region and

the intrinsic conductivity in the high- temperature region, respectively.

4. Discussion

As mentioned above, the oxygen-free NbMoTaWV thin film has a single BCC structure (a principal cluster is [m-m_{14}]). But with the increase of the solid-solution oxygen content ([O-m_6] clusters) in the films, the grains breaks, and the grain size decreases due to the crystal lattice expansion, which will enhance the solid-solution or grain-boundary strengthening. Eventually, both the hardness and modulus of films gradually increase. Meanwhile, electron scattering is strengthened due to the interstitial solid solution and the increasing grain boundaries. For the film with the 25 at.% oxygen, the solid-solution strengthening reaches the theoretical limit. With the increase of the oxygen content, [O-m_6] clusters gradually decrease, and [m-O_6] clusters begins to appear, resulting in the hardness and modulus of the films decrease. The content of [O-m_6]O_1 and [m-O_6]m_2 is theoretically equivalent when the oxygen content reaches 47 at.%. Further increasing the oxygen content, the principal clusters will become [m-O_6] clusters. The properties of the thin film will change from metallic to oxide semiconductor (approximately the ionic crystal) characteristics. The resistivity of the thin film containing the 50.93 at.% oxygen increases sharply, which confirms the properties of the films changed (Fig. 5).

4.1. Resistivity-temperature behavior of thin films

4.1.1. Films with metal characteristics

The resistivity-temperature curves of the $M_{100-x}O_x$ ($x < 43.2$) films show a plateau in the initial temperature rising stage (Fig. 7). Here, the width of the plateau represents the temperature range of the resistivity stability. The results exhibit that the plateau becomes narrower with increasing the oxygen content, indicating the decreasing resistivity stability. For the NbMoTaWV high-entropy film, the plateau width is larger than the others, such as AlCoCrFeNi [32], due to the microstructure stability caused by the increasing entropy, and the high-temperature stability brought by the high melting points of the five refractory elements.

The resistivity decreases rapidly with increasing temperature after the plateau stage, which is a common phenomenon in the disordered solid solution and amorphous [33]. Because diffusion is easier at high temperatures, resulting in the disordered-ordered transformation (phase transition or amorphous crystallization) of the structure. Here, the GIXRD analysis was performed on the two typical films ($M_{83.63}O_{16.37}$ and $M_{56.80}O_{43.20}$) after the variable temperature resistivity measurement to explore the transformation of the film structure at high temperatures, as shown in Fig. 8. The structures of the two films are a BCC structure and nanocrystalline + amorphous structure, respectively. However, after the variable temperature resistivity measurement, in the $M_{83.63}O_{16.37}$ thin film, the BCC diffraction peaks disappear, and new diffraction peaks appear at 26.7°, 35.6°, and 53.2°, respectively, while the $M_{56.80}O_{43.20}$ thin film is crystallized obviously, and the positions of the crystallization peaks are the same as the $M_{83.63}O_{16.37}$ film. The pattern after the variable temperature resistivity test was fully fitted by the JADE software [34], it is found that the new diffraction peaks corresponds to the TiO_2 type structure through referencing the existing structure of the single-cationic oxide. By comparing and analyzing the PDF card (PDF#82-1142, 89-4773, and 79-1655) and the Pearson Handbook of Crystallography (No.136MoO_2 and No.136WO_2), this structure oxide is present in all five single cationic oxides, Hence, it is determined that a metal oxide with a single TiO_2 structure is formed in the thin films after the variable temperature resistivity test.

4.1.2. Films with amorphous oxide semiconductors

For the films with oxygen contents greater than about 47 at.%, they have an amorphous structure. Generally, as the temperature increases, the resistivity must decrease continuously along with the process of amorphous-film crystallization from disorder to order. However, the Lnσ - $1/T$ curves of the $M_{49.07}O_{50.93}$ and $M_{46.37}O_{53.63}$ amorphous films shows two slopes at different temperature stages [Fig. 7(b)], which can be judged from the curve shape that the resistivity-temperature behavior of films is similar to that of ionic crystals.

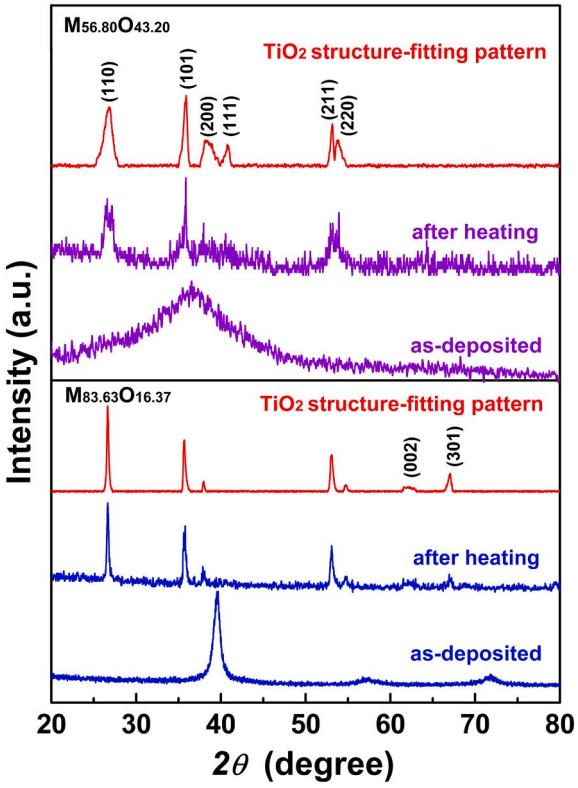

Fig. 8. XRD patterns of $M_{83.63}O_{16.37}$ and $M_{56.80}O_{43.20}$ thin films before and after the measurement of the temperature-variable resistance, and the fitting pattern of the TiO_2 structure.

From the point of view of the structure, the two amorphous films can be crystallized into oxides of the TiO_2 structure (a typical ionic crystal structure), which indicated that the correlation between amorphous films and ionic crystal structures. Based on the cluster theory, the crystallized structure will inherit the local structure (principal cluster) of the amorphous, which is the basis for the similar properties of the amorphous and the crystalline structures [35]. Therefore, it is logical to select the principal cluster of the amorphous structure by the crystallized structure, the cluster formula of the amorphous film can only be [m-O_6]m_2 from the crystal structure of TiO_2.

The conductive behavior of metal-ion crystals with the temperature can be divided into two parts: the impurity conduction at low temperatures where the impurity is the main carrier, and the intrinsic conduction at high temperatures in which ions or vacancies become conducting carriers under the action of the electric field [36]. At high temperatures, the effect of ionic properties and crystal structures on the ionic conductivity through changing the conductive activation energy (E_a) is achieved. The E_a is related to the slope of the conductivity-temperature curve and obeys the Arrhenius formula, which can be described by the following formula [37,38].

$$\sigma T = A exp\left(\frac{-E_a}{k_B T}\right) \quad (1)$$

where σ is the conductivity, A is a constant, T is the absolute temperature, k_B is the Boltzmann constant, and k_B equal to 0.026 eV. For convenience of calculations, taking the napierian logarithm of both

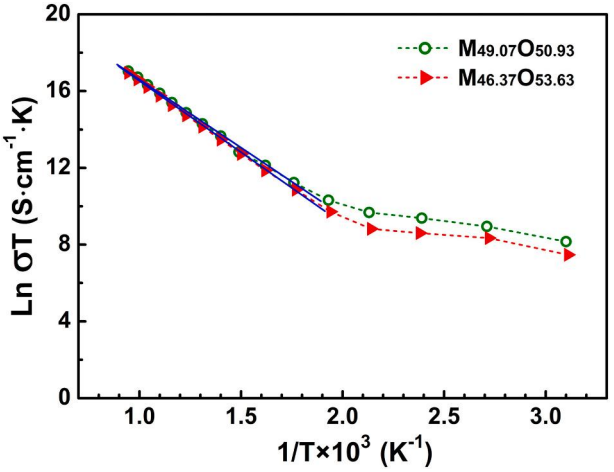

Fig. 9. LnσT - $1/T$ curves of the $M_{49.07}O_{50.93}$ and $M_{46.37}O_{53.63}$ thin films.

sides of Eq. (1), as shown in the Eq. (2):

$$Ln\ \sigma T = \frac{-E_a}{k_B T} \tag{2}$$

The LnσT - $1/T$ curves of the $M_{49.07}O_{50.93}$ and $M_{46.37}O_{53.63}$ thin films are presented in Fig. 9. At the high temperature stage, the E_a of the two films were calculated to be 0.18 eV and 0.20 eV, respectively, which indicates that the E_a slightly increases but the electrical conductivity weakens with increasing the oxygen content. The oxygen content of the single-metal oxide VO is similar to those of the $M_{49.07}O_{50.93}$ and $M_{46.37}O_{53.63}$ thin films, but its E_a is only 7×10^{-3} eV [39]. Obviously, the formation of the high-entropy alloy oxide can greatly increase the E_a and reduce the σ.

In summary, the conduction mechanism changes with the variation of the composition. Meanwhile, with the increase of the oxygen content, the film changes from the metallic oxygen-containing solid solution to the semiconductor amorphous oxide (similar to TiO_2 type ionic crystal).

4.2. Strengthening mechanisms

Based on the microstructural characterization of $M_{100-x}O_x$ (x = 0–53.63) films and the analysis from Fig. 5, it can be seen that the grain size of nanocrystalline decreases as the oxygen content increases. Furthermore, the microstructure of the film gradually translates from the crystalline to the amorphous state in the following order: nanocrystalline (tens of nanometers to several nanometers) → nanocrystalline (several nanometers) and partial amorphous → amorphous. Here, three typical samples ($M_{91.84}O_{8.16}$, $M_{78.46}O_{21.54}$, and $M_{46.37}O_{53.63}$) were selected for the discussion to deeply understand the strengthening mechanism of $M_{100-x}O_x$ (x = 0–53.63) films.

4.2.1. $M_{91.84}O_{8.16}$ thin film

The $M_{91.84}O_{8.16}$ film is composed of single-phase BCC nanocrystalline. Therefore, grain-boundary strengthening and solid-solution strengthening are considered as the main strengthening mechanisms, which are elaborated as follows.

(1) Grain-boundary strengthening

With the refinement of grains, more grain boundaries are introduced, which hinders the movement of dislocations within the grain, thereby increasing the yield strength. The average grain sizes of $M_{91.84}O_{8.16}$ film is 40 nm. The strengthening effect (σ_{gb}) due to the decrease in the grain size of bcc phase can be calculated according to the Hall-Petch equation [40,41]:

Table 2
Contributions of different strengthening mechanisms for the $M_{100-x}O_x$ films strength.

Films	σ_{gb} (GPa)	$\Delta\sigma_{ss}$ (GPa)	σ_{total} (GPa)	Hv ≈ $3\sigma_{total}$ (GPa)	Measured value Hv (GPa)
$M_{91.84}O_{8.16}$	4.00	0.78	4.78	14.34	13.33
$M_{78.46}O_{21.54}$	4.29	1.26	5.55	16.65	15.50
$M_{46.37}O_{53.63}$				9.50	9.82

$$\sigma_{gb} = \sigma_0 + kd^{-1/2} \tag{3}$$

where σ_0 is the lattice friction stress, equal to 2160 ± 130 MPa, k is the strengthening coefficient, equal to 0.44 ± 0.015 MPa $m^{1/2}$, and d is the average grain size [42,43]. By calculations, σ_{gb} is 4.0 GPa (as shown in Table 2).

(2) Solid-solution strengthening

In NbMoTaWV films, Oxygen can be dissolved in the BCC matrix by means of interstitial solid solution. Interstitials in BCC metals usually produce a tetragonal distortion of the lattice, which can give rise to a relatively large shear strain due to the interaction between dislocations and the tetragonal defects. The strength increment caused by interstitial solid solution $\Delta\sigma_{ss}$ is proportional to interstitial content and can be estimated as follows [44,45]:

$$\Delta\sigma_{ss} = \frac{G\Delta\varepsilon c^{1/2}}{3} \tag{4}$$

$$G = \frac{E}{2(1+\nu)} \tag{5}$$

where G is the shear modulus of BCC matrix. ν is Poisson's ratio (ν = 0.3) [46], and the E is the Young's modulus of BCC matrix, equal to 212 GPa, obtained from nanoindentation measurements. Therefore, the shear modulus of BCC matrix can be calculated, equal to 81.54 GPa. $\Delta\varepsilon$ is the difference between the longitudinal and transverse strain of the tetragonal distortion source when interstitial atoms occupy the interstitial sites in alloys, the calculated values of the tetragonal distortion $\Delta\varepsilon$ for the O is 0.10 [47], and c is the atomic concentration of interstitial atoms creating such defects. According to these parameters, the $\Delta\sigma_{ss}$ of $M_{91.84}O_{8.16}$ thin film is 0.78 GPa.

4.2.2. $M_{78.46}O_{21.54}$ thin film

The microstructure of the $M_{78.46}O_{21.54}$ film also consists of single-phase BCC nanocrystalline, and the grain size is about 4 nm. Similar to the $M_{91.84}O_{8.16}$ film, grain-boundary strengthening and solid-solution strengthening are available to the film.

When the grain size is less than a critical grain size (~ 10 nm), the relationship between the yield strength and grain size do not obey the Hall-Petch relationship, which is expected to occur for most metals [48,49]. The reason is that the main deformation mechanism of the film changes from the dislocation glide to grain-boundary sliding [50,51]. The grain size of the $M_{78.46}O_{21.54}$ film is about 4 nm, which exhibits the inverse Hall-Petch behavior [52]. Therefore, the σ_{gb} can be calculated according to the following equation [53].

$$\sigma_{gb} = \sigma_0 + \frac{0.36}{\sqrt{d}} - \sigma_{in} f_{gb} \tag{6}$$

$$f_{gb} = 1 - (1 - w/d)^3 \tag{7}$$

where f_{gb} is the volume fraction of grain boundaries. It can be expressed by the following Eq. (7), w is the width of the grain boundary, which is approximately about 1 nm for the BCC structure, σ_{in} is the internal stress along the grain boundary that depends on parameters such as grain-boundary thickness, lattice distortions near grain boundaries, and grain size,

$$\sigma_{in} = \frac{2G_g\delta}{d} \quad (8)$$

where G_g is the shear modules of the grain next to grain boundaries,G_g = (60–75%)G; δ represents the distance of the mismatch or distortion in grains, $\delta = 0.8a$, a is the lattice constant (a = 0.3186 nm). By calculations, the σ_{gb} of the $M_{78.46}O_{21.54}$ film is 4.29 GPa. Meanwhile, According to the Eq. (4), the $\Delta\sigma_{ss}$ of the $M_{78.46}O_{21.54}$ thin film is 1.26 GPa, the results are shown in Table 2.

4.2.3. $M_{46.37}O_{53.63}$ thin film

When the oxygen content is above 47 at.%, the thin film is fully amorphous, which consists of a variety of metal oxides, and its hardness can be expressed by the following formula [54]:

$$H_V = C(\alpha GK)^{1/2} \quad (9)$$

where C is the proportional constant to give the ratio of the stress to the resistance to deformation at the time when the indentation ceases (C = 0.1), and α is bond strength factor. G and K are the shear modulus and bulk modulus, respectively. Eq. (9) shows that it is possible to estimate the hardness number of the film if both shear and bulk moduli and average single-bond strength are known for the given film. In an isotropic material, such as glass, both bulk and shear moduli are known to be related to Young's modulus and Poisson's ratio by the equations, the shear modulus is shown in Eq. 5, the bulk modulus can be expressed as:

$$K = \frac{E}{3(1-2\nu)} \quad (10)$$

The value of α, the ratio of the average single bond strength to m-O bond strength, can be given from Eq. (11), where f_j is the number of cations, j is the one mole weight of film, n_j is the coordination number, ε_j is the single bond strength of the cation j to the oxygen bond, and ε_0 is the single bond strength of the m-O bond. by calculations, α = 0.886.

$$\alpha = \frac{\Sigma\{f_j n_j \varepsilon_j\}}{\varepsilon_0 \Sigma\{f_j n_j\}} \quad (11)$$

The calculated value of hardness of $M_{46.37}O_{53.63}$ film is 9.50 GPa (as shown in Table 2) according to the above equations, which is in agreement with the provided measured value. For the $M_{91.84}O_{8.16}$ and $M_{78.46}O_{21.54}$ films, by calculations, the σ_{total} values are equal to 4.78 GPa and 5.55 GPa, respectively. Zhang et al. [55] has reported that the hardness approximates three times of the strength. Hence, the calculated values of hardness for the $M_{91.84}O_{8.16}$ and $M_{78.46}O_{21.54}$ films are 14.34 GPa and 16.65 GPa, respectively, there is a slight deviation from the measured value, which may be due to the measurement error of oxygen.

Comparing the contributions of different strengthening mechanisms, it was found that the main differences of strengthening mechanisms evidently resulted from the microstructure of $M_{100-x}O_x$ (x = 0–53.63) film gradually transitioning from the crystalline state to the amorphous state. The films with low oxygen contents (0–25 at.%) have an entire single-phase BCC nanocrystalline structure. The strengthening mechanisms are the grain-boundary strengthening and solid-solution strengthening. In particular, with increasing the oxygen content, the size of the nanocrystalline phase decreases, and more oxygen is dissolved into the NbMoTaWV matrix, which lead to reinforced solid-solution strengthening is reinforced and the grain boundary strengthening is compatible with the inverse Hall-Petch relationship rather than the Hall-Petch relationship. Further increasing the oxygen content, Amorphous structures begin to appear. When the oxygen content ranges from 25% to 47%, the films have a mixed amorphous-nanocrystalline structure, such as $M_{64.08}O_{35.92}$ and $M_{56.80}O_{43.20}$ films. The films can be regarded as a two-phase composite, and the hardness can be described by a simple rule-of-the-mixture [56]. When the oxygen content exceeds 47 at.%, the films only have an amorphous structure and is subject to the strengthening mechanism of the amorphous structure. The hardness of amorphous films is lower than crystalline films because of less dense packing in the amorphous state [57]. The hardness of films with different oxygen content were calculated, there is a slight deviation from the measured value. However, it can be found that the calculation result is consistent with the change trend of measured hardness.

5. Conclusions

In order to investigate the properties and local structural evolution of refractory high-entropy alloy oxide films with different oxygen contents, $M_{100-x}O_x$ (x = 0–53.63) films were deposited on a single-crystal Si (100) substrate by RF magnetron sputtering, and the cluster-plus-glue-atom model were introduced to interpret the compositions of films. With increasing the oxygen content, the local structure of films gradually changed from [m-m_{14}] to [O-m_6], and finally to the amorphous oxide structure of [m-O_6]. The hardness and modulus increase first and then decrease with a range of 9.8–15.5 GPa and 179.4–215.6 GPa, respectively. The RT resistivity of the film continuously rises from 55 to 1.26 × 10^6 μΩ·cm, and the rising rate is relatively large at high oxygen content. Particularly, the $M_{78.46}O_{21.54}$ film with a fine nanocrystalline structure shows the best comprehensive properties, the hardness can reach 15.5 GPa and the resistivity is about 355 μΩ·cm. With increasing the oxygen content, the strengthening mechanism of the film changes from grain-boundary strengthening and solid-solution strengthening, to a pure amorphous strengthening mechanism. The conductive mechanism transforms from a metal solid solution to an amorphous oxide semiconductor (similar to TiO_2 type ionic crystal). The $M_{100-x}O_x$ films have a broad application prospect, which could be modulated in a wide range, covering conductors to semiconductors.

CRediT authorship contribution statement

Linxia Bi:Writing - original draft, Data curation, Investigation, Formal analysis.**Xiaona Li**:Conceptualization, Methodology, Formal analysis, Supervision.**Zhumin Li**:Writing - review & editing, Formal analysis.**Yinglin Hu**:Writing - review & editing.**Junyi Zhang**:Conceptualization, Writing - review & editing.**Qing Wang**:Conceptualization, Writing - review & editing.**Chuang Dong**:Conceptualization, Writing - review & editing.**Yuehong Zheng**:Conceptualization, Writing - review & editing.**Peter K. Liaw**:Supervision, Writing - review & editing.

Declaration of competing interest

The work described has not been published before; it is not under consideration for publication anywhere else; and publication has been approved by all co-authors and the responsible authorities at the institute where the work has been carried out.

Acknowledgements

We gratefully acknowledge the financial supports by the National Natural Science Foundation of China [U1867201], the Fundamental Research Funds for the Central Universities (Grant No. DUT17LAB09), the Science Challenge Project (TZ2016004), & the National Science Foundation (DMR-1611180 and 1809640) with the program directors, Drs G. Shiflet and D. Farkas.

References

[1] C.M. Rost, E. Sachet, T. Borman, A. Moballegh, E.C. Dickey, D. Hou, J.L. Jones, S. Curtarolo, J.P. Maria, Entropy-stabilized oxides, Nat. Commun. 6 (2015) 8485, https://doi.org/10.1038/ncomms9485.

[2] J.L. Braun, C.M. Rost, M. Lim, A. Giri, D.H. Olson, G.N. Kotsonis, G. Stan, D.W. Brenner, J.P. Maria, P.E. Hopkins, Charge-induced disorder controls the thermal conductivity of entropy-stabilized oxides, Adv. Mater. 30 (2018) 1805004, , https://doi.org/10.1002/adma.201805004.

[3] A. Kirnbauer, C. Spadt, C.M. Koller, S. Kolozsvári, P.H. Mayrhofer, High-entropy oxide thin films based on Al-Cr-Nb-Ta-Ti, Vacuum 168 (2019) 108850, https://doi.org/10.1016/j.vacuum.2019.108850.

[4] K.R. Wu, C.H. Ting, J.J. Wang, W.C. Liu, C.H. Lin, Characteristics of graded TiO_2 and TiO_2/ITO films prepared by twin DC magnetron sputtering technique, Surf. Coat. Technol. 200 (2006) 6030–6036, https://doi.org/10.1016/j.surfcoat.2005.09.031.

[5] M. Sridharan, M. Sillassen, J. Bøttiger, J. Chevallier, H. Birkedal, Pulsed DC magnetron sputtered Al_2O_3 films and their hardness, Surf. Coat. Technol. 202 (2007) 920–924, https://doi.org/10.1016/j.surfcoat.2007.05.061.

[6] N. Qiu, H. Chen, Z.M. Yang, S. Sun, Y.H. Wang, Y.H. Cui, A high entropy oxide ($Mg_{0.2}Co_{0.2}Ni_{0.2}Cu_{0.2}Zn_{0.2}O$) with superior lithium storage performance, J. Alloys Compd. 777 (2019) 767–774, https://doi.org/10.1016/j.jallcom.2018.11.049.

[7] D. Bérardan, S. Franger, A.K. Meena, N. Dragoe, Room temperature lithium superionic conductivity in high entropy oxides, J. Mater. Chem. A 4 (2016) 9536–9541, https://doi.org/10.1039/c6ta03249d.

[8] D. Bérardan, S. Franger, D. Dragoe, A.K. Meena, N. Dragoe, Colossal dielectric constant in high entropy oxides, Phys. Status Solidi (RRL) 10 (2016) 328–333, https://doi.org/10.1002/pssr.201600043.

[9] S. Zhai, J. Rojas, N. Ahlborg, K. Lim, M.F. Toney, H. Jin, W.C. Chueh, A. Majumdar, Use of poly-cation oxides to lower the temperature of two-step thermochemical water splitting, Emergy. Environ. Sci. 11 (2018) 2172–2178, https://doi.org/10.1039/C8EE00050F.

[10] K.P. Chen, X.T. Pei, L. Tang, H.R. Cheng, Z.M. Li, C.W. Li, X.W. Zhang, L.N. An, A five-component entropy-stabilized fluorite oxide, J. Eur. Ceram. Soc. 38 (2018) 4161–4164, https://doi.org/10.1016/j.jeurceramsoc.2018.04.063.

[11] Z.F. Lei, X.J. Liu, R. Li, H. Wang, Y. Wu, Z.P. Lu, Ultrastable metal oxide nanotube arrays achieved by entropy-stabilization engineering, Scr. Mater. 146 (2018) 340–343, https://doi.org/10.1016/j.scriptamat.2017. 12.025.

[12] F. Kurdesau, G. Khripunov, A.F. da Cunha, M. Kaelin, A.N. Tiwari, Comparative study of ITO layers deposited by DC and RF magnetron sputtering at room temperature, J. Non-Cryst. Solids 352 (2006) 1466–1470, https://doi.org/10.1016/j.jnoncrysol.2005.11.088.

[13] J.O. Park, J.H. Lee, J.J. Kim, S.H. Cho, Y.K. Cho, Crystallization of indium tin oxide thin films prepared by RF-magnetron sputtering without external heating, Thin Solid Films 474 (2005) 127–132, https://doi.org/10.1016/j.tsf.2004.08.172.

[14] M.I. Lin, M.H. Tsai, W.J. Shen, J.W. Yeh, Evolution of structure and properties of multi-component ($AlCrTaTiZr)O_x$ films, Thin Solid Films 518 (2010) 2732–2737, https://doi.org/10.1016/j.tsf.2009.10.142.

[15] M.C. Gao, J.W. Yeh, P.K. Liaw, Y. Zhang, High-entropy Alloys, Springer International Publishing, Switzerland, 2016.

[16] X.B. Feng, J.Y. Zhang, Y.Q. Wang, Z.Q. Hou, K. Wu, G. Liu, J. Sun, Size effects on the mechanical properties of nanocrystalline NbMoTaW refractory high entropy alloy thin films, Int. J. Plast. 95 (2017) 264–277, https://doi.org/10.1016/j.ijplas.2017.04.013.

[17] O.N. Senkov, G.B. Wilks, J.M. Scott, D.B. Miracle, Mechanical properties of $Nb_{25}Mo_{25}Ta_{25}W_{25}$ and $V_{20}Nb_{20}Mo_{20}Ta_{20}W_{20}$ refractory high entropy alloys, Intermetallics 19 (2011) 698–706, https://doi.org/10.1016/j.intermet.2011.01.004.

[18] Y.Y. Chen, S.B. Hung, C.J. Wang, W.C. Wei, J.W. Lee, High temperature electrical properties and oxidation resistance of V-Nb-Mo-Ta-W high entropy alloy thin films, Surf. Coat. Technol. 375 (2019) 854–863, https://doi.org/10.1016/j.surfcoat.2019.07.080.

[19] S.B. Hung, C.J. Wang, Y.Y. Chen, J.W. Lee, C.L. Li, Thermal and corrosion properties of V-Nb-Mo-Ta-W and V-Nb-Mo-Ta-W-Cr-B high entropy alloy coatings, Surf. Coat. Technol. 375 (2019) 802–809, https://doi.org/10.1016/j.surfcoat.2019.07.079.

[20] C. Dong, Q. Wang, J.B. Qiang, Y.M. Wang, N. Jiang, G. Han, Y.H. Li, J. Wu, J.H. Xia, From clusters to phase diagrams: composition rules of quasicrystals and bulk metallic glasses, J. Phys. D. Appl. Phys. 40 (2007) R273–R291, https://doi.org/10.1088/0022-3727/40/15/R01.

[21] K. Shimanovich, Y. Bouhadana, D.A. Keller, S. Rühle, A.Y. Anderson, A. Zaban, Four-point probe electrical resistivity scanning system for large area conductivity and activation energy mapping, Rev. Sci. Instrum. 85 (2014) 055103, , https://doi.org/10.1063/1.4873353.

[22] Q. Xiao, Y. Sun, J. Zhang, Q.J. Li, Size-dependent of chromium (VI) adsorption on nano α-Fe_2O_3 surface, Appl. Surf. Sci. 356 (2015) 18–23, https://doi.org/10.1016/j.apsusc.2015.08.005.

[23] X.N. Li, L.J. Jin, Y.H. Zheng, Q. Wang, C. Dong, Composition range of semiconducting amorphous Fe-Si thin films interpreted using a cluster-based short-range-order model, J. Alloys Compd. 706 (2017) 495–501, https://doi.org/10.1016/j.jallcom.2017.02.255.

[24] Y. Ma, Q. Wang, C.L. Li, L.J. Santodonato, M. Feygenson, C. Dong, P.K. Liaw, Chemical short-range orders and the induced structural transition in high-entropy alloys, Scr. Mater. 144 (2018) 64–68, https://doi.org/10.1016/j.scriptamat.2017.09.049.

[25] J.X. Chen, Q. Wang, Y.M. Wang, J.B. Qiang, C. Dong, Cluster formulae for alloy phases, Philos. Mag. Lett. 90 (2010) 683–688, https://doi.org/10.1080/09500839.2010.495356.

[26] G. Han, J.B. Qiang, F.W. Li, L. Yuan, S.G. Quan, Q. Wang, Y.M. Wang, C. Dong, P. Häussler, The *e/a* values of ideal metallic glasses in relation to cluster formulae, Acta Mater. 59 (2011) 5917–5923, https://doi.org/10.1016/j.actamat.2011.05.065.

[27] Y.P. Ma, D.D. Dong, A.M. Wu, C. Dong, Composition formulas of inorganic compounds in terms of cluster plus glue atom model, Inorg. Chem. 57 (2018) 710–717, https://doi.org/10.1021/acs.inorgchem.7b02549.

[28] C. Pang, Q. Wang, R.Q. Zhang, Q. Li, X. Dai, C. Dong, P.K. Liaw, β Zr–Nb–Ti–Mo–Sn alloys with low Young's modulus and low magnetic susceptibility optimized via a cluster-plus-glue-atom model, Mater. Sci. Eng. A 626 (2015) 369–374, https://doi.org/10.1016/j.msea.2014.12.082.

[29] C. Pang, B.B. Jiang, Y. Shi, Q. Wang, C. Dong, Cluster-plus-glue-atom model and universal composition formulas [cluster](glue atom)$_x$ for BCC solid solution alloys, J. Alloys Compd. 652 (2015) 63–69, https://doi.org/10.1016/j.jallcom.2015.08.209.

[30] P. Bonasewicz, W. Hirschwald, G. Neumann, The investigation of the pressure and temperature dependence of the electrical conductivity of thin zinc oxide films with high resistances, Phys. Status. Solidi. A. 97 (1986) 593–599, https://doi.org/10.1002/pssa.2210970234.

[31] R.F. Janninck, D.H. Whitmore, Electrical conductivity and thermoelectric power of niobium dioxide, J. Phys. Chem. Solids 27 (1966) 1183–1187, https://doi.org/10.1016/0022-3697(66)90094-1.

[32] C.Y. Wang, X.N. Li, Z.M. Li, Q. Wang, Y.H. Zheng, Y. Ma, L.X. Bi, Y.Y. Zhang, X.H. Yuan, X. Zhang, C. Dong, P.K. Liaw, The resistivity-temperature behavior of $Al_xCoCrFeNi$ high-entropy alloy films, Thin Solid Films (2020) 137895, https://doi.org/10.1016/j.tsf.2020.137895.

[33] P.J. Cote, L.V. Meisel, Resistivity in amorphous and disordered crystalline alloys, Phys. Rev. Lett. 39 (1977) 102–105, https://doi.org/10.1103/PhysRevLett.39.102.

[34] T.P. Chou, Q.F. Zhang, G.E. Fryxell, G.Z. Cao, Hierarchically structured ZnO film for dye-sensitized solar cells with enhanced energy conversion efficiency, Adv. Mater. 19 (2007) 2588–2592, https://doi.org/10.1002/adma.200602927.

[35] H. Tian, C. Zhang, J.J. Zhao, C. Dong, B. Wen, Q. Wang, First-principle study of the structural, electronic, and magnetic properties of amorphous Fe-B alloys, Phys. B Condens. Matter 407 (2012) 250–257, https://doi.org/10.1016/j.physb.2011.10.042.

[36] R.W. Dreyfus, A.S. Nowick, Ionic conductivity of doped NaCl crystals, Phys. Rev. 126 (1962) 1367–1377, https://doi.org/10.1103/PhysRev.126.1367.

[37] R. Chiba, F. Yoshimura, J. Yamaki, T. Ishii, T. Yonezawa, K. Endou, Ionic conductivity and morphology in Sc_2O_3 and Al_2O_3 doped ZrO_2 films prepared by the sol-gel method, Solid State Ionics 104 (1997) 259–266, https://doi.org/10.1016/S0167-2738(97)00423-2.

[38] X.X. Xu, Z.Y. Wen, X.L. Yang, J.C. Zhang, Z.H. Gu, High lithium ion conductivity glass-ceramics in Li_2O-Al_2O_3-TiO_2-P_2O_5 from nanoscaled glassy powders by mechanical milling, Solid State Ionics 177 (2006) 2611–2615, https://doi.org/10.1016/j.ssi.2006.04.010.

[39] N.F. Mott, Conduction in non-crystalline systems: VIII. The highly correlated electron gas in doped semiconductors and in vanadium monoxide, Philos. Mag. 24 (1971) 935–958, https://doi.org/10.1080/14786437108217059.

[40] E.O. Hall, The deformation and ageing of mild steel: III discussion of results, Proc. Phys. Soc. B. 64 (1951) 747–753, https://doi.org/10.1088/0370-1301/64/9/303.

[41] N.J. Petch, The cleavage strength of polycrystals, J. Iron. Steel. Inst. 174 (1953) 25–28.

[42] R.A. Masumura, P.M. Hazzledine, C.S. Pande, Yield stress of fine grained materials, Acta Mater. 46 (1998) 4527–4534, https://doi.org/10.1016/S1359-6454(98)00150-5.

[43] Y. Long, X.B. Liang, K. Su, H.Y. Peng, X.Z. Li, A fine-grained NbMoTaWVCr refractory high-entropy alloy withultra-high strength: microstructural evolution and mechanical properties, J. Alloys Compd. 780 (2019) 607–617, https://doi.org/10.1016/j.jallcom.2018.11.318.

[44] T.H. Courtney, Mechanical Behavior of Materials, Waveland Press, 2005.

[45] V. Keryvin, V.H. Hoang, J. Shen, Hardness, toughness, brittleness and cracking systems in an iron-based bulk metallic glass by indentation, Intermetallics 17 (2009) 211–217, https://doi.org/10.1016/j.intermet.2008.08.017.

[46] A.S. Khan, R.Q. Liang, Behaviors of three BCC metal over a wide range of strain rates and temperatures: experiments and modeling, Int. J. Plast. 15 (1999) 1089–1109, https://doi.org/10.1016/S0749-6419(99) 00030-3.

[47] Z.F. Lei, X.J. Liu, Y. Wu, et al., Enhanced strength and ductility in a high-entropy alloy via ordered oxygen complexes, Nature 563 (2018) 546–550, https://doi.org/10.1038/s41586-018-0685-y.

[48] T.G. Nieh, J. Wadsworth, Hall-Petch relation in nanocrystalline solids, Scr. Met. Mater. 25 (1991) 955–958, https://doi.org/10.1016/0956-716X(91)90256-Z.

[49] J. Eckert, J.C. Holzer, C.E. Krill, W.L. Johnson, Reversible grain size changes in ball-milled nanocrystalline Fe-Cu alloys, J. Mater. Res. 7 (1992) 1980–1983, https://doi.org/10.1557/JMR.1992.1980.

[50] H. Van Swygenhoven, P.M. Derlet, Grain-boundary sliding in nanocrystalline fcc metals, Phys. Rev. B 64 (2001) 224105, , https://doi.org/10.1103/PhysRevB.64.224105.

[51] J. Schiøtz, F.D. Di Tolla, K.W. Jacobsen, Softening of nanocrystalline metals at very small grain sizes, Nature 391 (1998) 561–563, https://doi.org/10.1038/35328.

[52] C.C. Koch, J. Narayan, The inverse Hall-Petch effect—fact or artifact? Mat. Res. Soc. Symp. 634 (2000) B5.1.1–11, https://doi.org/10.1557/PROC-634-B5.1.1.

[53] A.S. Mohammadabadi, K. Dehghani, A new model for inverse Hall-Petch relation of nanocrystalline materials, J. Mater. Eng. Perform. 17 (2008) 662–666, https://doi.org/10.1007/s11665-008-9206-8.

[54] M. Yamane, J.D. Mackenzie, Vicker's hardness of glass, J. Non-Cryst. Sol. 15 (1974) 153–164, https://doi.org/10.1016/0022-3093(74)90044-1.

[55] P. Zhang, S.X. Li, Z.F. Zhang, General relationship between strength and hardness, Mater. Sci. Eng. A 529 (2011) 62–73, https://doi.org/10.1016/j.msea.2011.08.061.

[56] J.E. Carsley, J. Ning, W.W. Milligan, S.A. Hackney, E.C. Aifantis, A simple, mixtures-based model for the grain size dependence of strength in nanophase metals, Nanostruct. Mater. 5 (1995) 441–448, https://doi.org/10.1016/0965-9773(95)00257-F.

[57] H. Somekawa, T.G. Niehb, K. Higashia, Instrumented indentation properties of electrodeposited Ni-W alloys with different microstructures, Scr. Mater. 50 (2004) 1361–1365, https://doi.org/10.1016/j.scriptamat. 2004.02.042.